Available online at www.sciencedirect.com
ScienceDirect
Trans. Nonferrous Met. Soc. China 32(2022) 1881−1895
Transactions of Nonferrous Metals Society of China
www.tnmsc.cn

Microstructure and corrosion behaviors of as-rolled Mg−Zn−Er alloy sheets

Ke LIU, Feng LOU, Jun-jian FU, Zi-jian YU, Shu-bo LI, Zhao-hui WANG, Xian DU, Wen-bo DU

Faculty of Materials and Manufacturing, Beijing University of Technology, Beijing 100124, China

Received 18 June 2021; accepted 8 December 2021

Abstract: The corrosion behaviors and mechanism of the as-rolled Mg−*x*Zn−0.5Er (*x*=0.5, 2.0, 3.0 and 4.0, in wt.%) alloys were investigated. The potential difference between the second phase and matrix was determined by the type and size of the second phases. The dominated nano-scale *W*-phase on matrix in the Mg−0.5Zn−0.5Er alloy induced a sharp local pitting corrosion. However, as the volume fraction of the coarse *W*-phase or *I*-phase increased, the corrosion reaction was inclined to happen around the coarse *W*-phase or *I*-phase preferentially, leading to an obvious uniform corrosion and great acceleration of corrosion rate. The long-term immersion (14 d) results indicated that the corrosion resistance decreasing sequence was Mg−0.5Zn−0.5Er > Mg−2.0Zn−0.5Er > Mg−3.0Zn−0.5Er > Mg−4.0Zn−0.5Er.
Key words: magnesium alloys; second phases; microstructure; corrosion behavior

1 Introduction

As the lightest structural materials, magnesium and its alloys exhibit excellent characters of high specific strength, high specific stiffness, good shock absorption capability, good process ability and biocompatibility [1−3]. They have potential application prospects in automobile parts, portable electronic devices, biodegradable implants and so on [4−6]. Nonetheless, the practical applications of magnesium alloys are limited because of their relatively poor corrosion resistance [7−9]. Magnesium alloys are usually inclined to react with other substances, such as oxygen and chlorine gases, which are prone to corrode the matrix by reacting with water or other common acids at room temperature. It is well known that the standard electrode potential of the magnesium is about −2.36V (vs NHE), which is the lowest in common metals [10,11]. The oxide film formed naturally in air is mainly composed of MgO, and the film formed in the aqueous solution is made up of $Mg(OH)_2$ [3,12]. The P/B mass ratios of these films are less than 1, and their surface films are not chemically stable and susceptible to dissolution in corrosive electrolytes, resulting in ineffective protection for substrates [13].

Alloying is an effective way to improve corrosion resistance via enhancing corrosion potential of magnesium alloys [14]. However, excessive addition of elements usually leads to lots of second phases, such as the popular LPSO-phase, *I*-phase and *W*-phase in Mg−Zn−RE alloys, and these phases played an important role in mechanical properties [15]. Most of the previous studies mainly concentrated on the effects of these second phases on mechanical properties, but neglected corrosion behaviors of magnesium alloys. The second phases precipitated during solidification would activate the micro-galvanic corrosion of neighboring matrix grains because of their high potential difference with matrix, which was one of the most important factors to affect the corrosion rate and corrosion

Corresponding author: Ke LIU, Tel/Fax: +86-10-67392423, E-mail: lk@bjut.edu.cn
DOI: 10.1016/S1003-6326(22)65915-6

mechanism of magnesium alloys [16,17].

Recently, a few researchers have paid attention to investigating the second phases on corrosion performance of magnesium alloys. In the Mg−Zn binary alloys, it was found that the coarse Mg_xZn_y phases as strong cathodic sites resulted in dramatical pitting corrosion, and the corrosion rate was related to the volume fraction of these phases significantly in the corrosive condition [18,19]. Also, the coarse $Mg_{17}Al_{12}$ phase (β-phase) accelerated corrosion rate by micro-galvanic coupling between the matrix and this phase [20]. Now, a new report suggested that the local potential decreasing sequence was LPSO-phase < *I*-phase < *W*-phase, and the Mg−Zn−Gd−Zr alloys containing *W*-phase suffered from a drastic corrosion reaction by strong micro-galvanic corrosion [21]. To some extent, this sequence just stood for the corrosion tendency (capability) of the second phases. In fact, the actual micro-galvanic corrosion performance of the magnesium alloys was determined by lots of other factors such as volume fraction, morphology (size) and distribution of second phases, which significantly affected the corrosion rates of magnesium alloys actually and should be considered comprehensively in future work. If not, it was ineffective to escape the contradictory results, for instance, the effects of $Mg_{17}Al_{12}$ phase (β-phase) in Al-containing magnesium alloys and LPSO-phase in Mg−Zn−RE alloys on corrosion resistance of magnesium alloys [8,16,22,23].

So, the present work aimed to systematically investigate effects of kinds, volume fraction, morphology (size) and distribution of the second phases on corrosion behaviors of Mg−Zn−Er alloys containing *W*-phase, *W*-phase + *I*-phase and *I*-phase, respectively. Therefore, four kinds of Mg−Zn−Er alloys were designed, i.e., Mg−0.5Zn−0.5Er alloys (only containing tiny *W*-phase, called Alloy A), Mg−2Zn−0.5Er alloys (containing *W*-phase, called Alloy B), Mg−3Zn−0.5Er alloys (containing *W*-phase + *I*-phase, called Alloy C) and Mg−4Zn−0.5Er alloys (containing *I*-phase, called Alloy D). In this work, one focus was the investigation on volume fraction, morphology (size) and distribution of the second phases on corrosion performance and corrosion mechanism during immersion test in 3.5 wt.% NaCl solution. The second focus was the investigation on potential difference between different (including kinds and size) second phases and matrix, providing straightforward experiment results for the corrosion performance of Mg−Zn−Er alloys. At last, the relationship between the corrosion performance and the second phases was discussed quantitatively.

2 Experimental

Mg−*x*Zn−Er (*x*=0.5, 2.0, 3.0 and 4.0, in wt.%) alloys were prepared by commercially pure magnesium (99.99 wt.%), pure zinc (99.99 wt.%) and Mg−30Er (wt.%) master alloy in this work. The alloys were produced in an electric resistance furnace accompanying with protecting gas consisting of 99 vol.% N_2 and 1 vol.% SF_6 during melting process. During melting, the Mg−30Er mater alloy and the iron mold were preheated at 200 °C. At 700 °C, the melts were poured into an iron mold, and the as-cast Mg−Zn−Er ingots with dimensions of 200 mm (length) × 120 mm (width) × 33 mm (thickness) were produced. The ingots were solution-treated in a resistance furnace for 10 h at 440 °C and then quenched into warm water at 75 °C. The solution-treated ingots were cut into plates with a thickness of 5 mm for a subsequent rolling process. The rolling experiments were carried out at 400 °C with a thickness of 8%−10% reduction per pass, and the rolling speed was kept at 7 m/min. Finally, the alloy sheets with a reduction of about 78% were produced. The actual compositions of these Mg−Zn−Er alloys were analyzed by fluorescence spectrometer (XRF), and the composition results are shown in Table 1.

Table 1 Chemical compositions of Mg−Zn−Er alloys

Sample	Chemical composition/wt.%			Zn/Er mass ratio
	Zn	Er	Mg	
Alloy A	0.62	0.56	Bal.	1.1
Alloy B	2.1	0.51	Bal.	4.1
Alloy C	3.2	0.56	Bal.	5.7
Alloy D	4.1	0.52	Bal.	7.9

The microstructure and microtexture of as-rolled Mg−Zn−Er alloys were observed from the RD−ND plane by using optical microscope (OM, Zeiss-Imager.A2m). The phase constituents were analyzed by using transmission electron microscope (TEM, JET−2100) equipped with energy dispersive spectroscope (EDS) and selected area electron

diffraction (SAED). The volume fractions of these second phases in as-rolled Mg−Zn−Er alloys were measured by using an image analysis method (Image Pro Plus 6.0). The surface morphology and corrosion products of as-rolled Mg−Zn−Er alloys were observed by using scanning electron microscope (SEM, JEM−7001F) and EDS. The relative potential differences between α-Mg and second phases were examined via scanning Kelvin probe force microscope (SKPFM, Nanoscope, SCM-PIT) at 25 °C in atmospheric conditions at a controlled relative humidity of (25±5)%. These samples for SKPFM observation were firstly mechanically polished, and then cleaned by ultrasonic with ethanol. In this work, a silicon tip with a 20 nm-thick platinum-coating was used as the reference electrode. The potential difference values were analyzed by Asylum research software.

The immersion tests were carried out in 3.5 wt.% NaCl solution. The immersion samples were cut from the as-rolled sheets with a surface area of 10 mm × 10 mm, and the thickness was ~1.1 mm. The samples were immersed into the corrosion medium at room temperature for 1, 3, 7 and 14 d, respectively. The products on the surface of samples were cleaned up with chromic acid solution (200 g/L CrO_3 + 10 g/L $AgNO_3$), then rinsed with ethanol, dried in air and finally weighed. The masses of samples before and after immersion were measured by a balance with an accuracy of 0.1 mg, respectively. The corrosion rate was calculated as the following equation:

$$C_R = \frac{Kw}{Atd} \quad (1)$$

where C_R is the corrosion rate (mm/a), K (=8.76×10^4) is the coefficient, w is the mass loss (g), A is the surface area exposed to the 3.5 wt.% NaCl solution (cm^2), t is the exposure time (h), and d is the density (g/cm^3).

The samples for electrochemical test were cut from as-rolled Mg−Zn−Er alloys, and were mounted by epoxy resins with an exposed surface area of 1 cm^2. This electrochemical test was based on the Auto lab electrochemical testing system (PGSTAT302N) companied with a three-electrode measurement system. The saturated calomel electrode (SCE) was the reference electrode. The platinum electrode was the counter electrode (CE) and the working electrode was the sample. The test was carried out at room temperature in 3.5 wt.% NaCl solution. The working electrode was firstly immersed in 3.5 wt.% NaCl solution, and the measurement began from the stabilization of the open circuit potential (OCP) for about 5 min. The polarization curve test was performed under the open circuit voltage of 300 mV at a scanning rate of 0.5 mV/s with the potential changing from −2.1 to −1.4 V. The electrochemical impedance spectroscopy (EIS) scan frequency was from 0.01 to 1.4 MHz with a perturbation amplitude of 5 mV. The corrosion potential (φ_{corr}), corrosion current density (J_{corr}) and electrochemical impedance spectroscopy (EIS) spectra were calculated by ZView 3.1 analyzer software. At least, three specimens were tested for each sample.

3 Results and discussion

3.1 Microstructure characterization

The OM microstructures from the RD−ND surface of as-rolled Mg−xZn−0.5Er (x=0.5, 2.0, 3.0 and 4.0, in wt.%) alloys are shown in Fig. 1. Partially recrystallized microstructures with twins and shear bands are present because of the severe deformation during multi-pass rolling process. The average grain sizes of Alloys A, B, C and D are 15.3, 23.8, 12.6 and 25.0 μm, respectively. The grain size is mainly determined by the dynamic recrystallization (DRX) which is related to the level of added Zn [24,25]. The addition of Zn leads to the formation of I-phase or W-phase, and these second phases also have a great effect on activating DRX via particle stimulated nucleation (PSN) [26,27].

The OM microstructures include varying amount of precipitates, and increasing numbers of particles are found as the addition of Zn increases. The volume fractions of these second phases in Alloys A, B, C and D are (0.25±0.03)%, (0.61±0.05)%, (0.78±0.07)% and (1.39±0.11)%, respectively. As marked by the red circles in Fig. 1(a), there are actually a few precipitates in Alloy A, and the orbicular precipitates mainly locate at the matrix with a size of 0.85−2.50 μm. When the content of Zn is more than 2.0 wt.%, there are two kinds of precipitates with orbicular and irregular morphologies in as-rolled Mg−xZn−0.5Er ($x \geq 2$) alloys, as shown in Figs. 1(b−d). The precipitates get coarse as the content of Zn increases. In Alloy D, the size of orbicular-type

particles is 1.0−3.5 μm, and the size of irregular-type precipitates located at grain boundaries is 4.00−20.00 μm in length and 1.50−8.00 μm in width, as seen in Fig. 1(d).

Figure 2 shows TEM images observed from as-rolled Mg−Zn−Er alloys. The SAED pattern (inserted in Fig. 2(a) at the upper-right corner) is corresponding to the orbicular-type phase in Zone *A*, which indicates that the crystal structure of this kind phase in Alloy A is a face centered cubic (FCC) structure. The EDS results are shown in Table 2. It is found that the average content of each element in Zone *A* is 60.16 at.% Mg, 25.58 at.% Zn, 14.26 at.% Er, and the Zn/Er molar ratio is 1.79:1. The Zn/Er molar ratio of the particles in Zone *B* in Fig. 2(a) is 1.64:1, which is apparent that the Zn/Er molar ratios of particles in Zones *A* and *B* are all close to 1.50:1, respectively. In summary, it is confirmed that the nano-scale phase in Alloy A is the *W*-phase. Figure 2(b) shows the TEM image

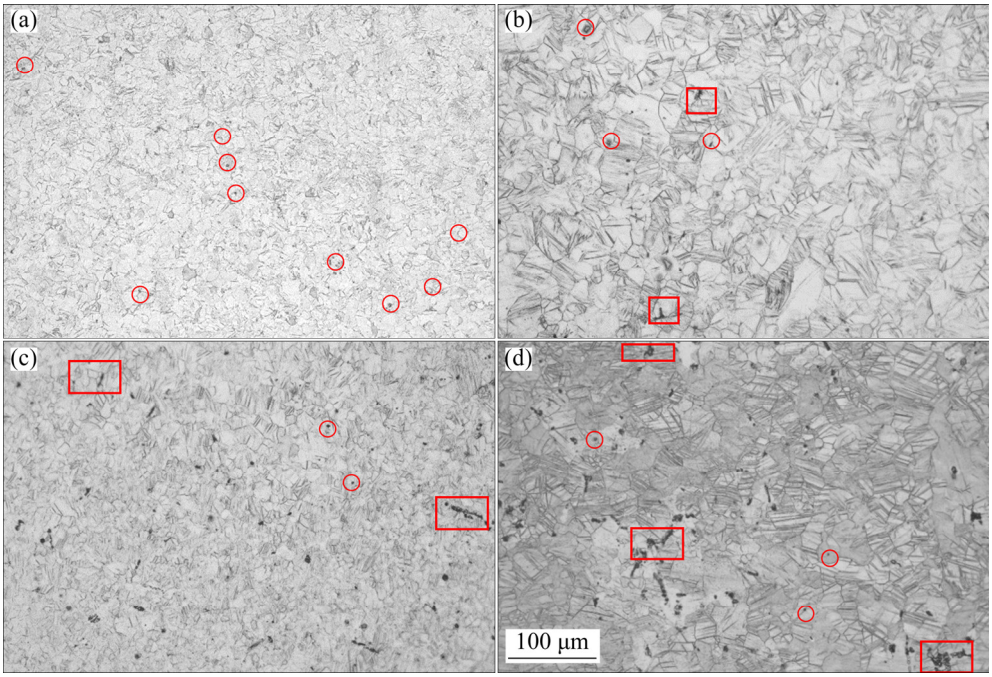

Fig. 1 OM images of Mg−Zn−Er alloys on RD−ND plane with thickness reduction of 78%: (a) Alloy A; (b) Alloy B; (c) Alloy C; (d) Alloy D

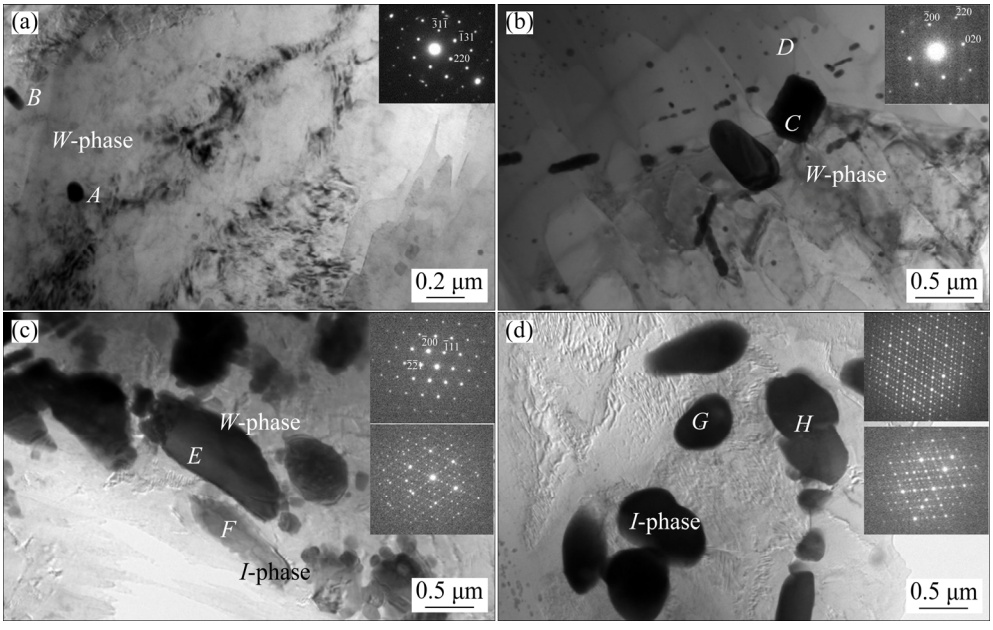

Fig. 2 TEM images of Mg−Zn−Er alloys: (a) Alloy A; (b) Alloy B; (c) Alloy C; (d) Alloy D

Table 2 EDS analysis results observed from as-rolled Mg−Zn−Er alloys (at.%)

Zone in Fig. 2	Mg	Zn	Er
A	60.16	25.58	14.26
B	81.88	11.26	6.87
C	55.95	28.53	15.52
D	83.8	10.75	5.45
E	31.19	44.96	23.85
F	41.89	50.47	7.65
G	30.96	56.57	12.47
H	30.26	59.52	10.22

of Alloy B. It can be seen that there are two kinds of particles with different morphologies. The primary coarse *W*-phase is broken into small-size particles with a size of 600 nm in length and 200−300 nm in width. The EDS result of the particle in Zone *C* is shown in Table 2. The Zn/Er molar ratio is 1.84:1, and the ratio agrees well with that of the *W*-phase. Besides, some nano-scale *W*-phase particles are found (Zone *D* in Fig. 2(b)). The size of the nano-scale *W*-phase was about 200 nm with a regular or oval morphology, respectively. The EDS results are shown in Table 2. Figure 2(c) shows the TEM image of Alloy C. The volume fraction of the broken phase is higher than that in Alloy B. It is found that Alloy C has two kinds of second phases which would be certified by SAED patterns and EDS results. One is the broken *W*-phase (FCC) which has a larger size. The other is the broken *I*-phase indicated by SAED pattern, and the pattern shows its own two-fold symmetry. Also, the EDS results of the *I*-phase and *W*-phase are shown in Table 2, respectively. Figure 2(d) shows the TEM image of the second phase in Alloy D. The coarse second phase is the *I*-phase which is confirmed by the SAED pattern (inset in Fig. 2(d)). The EDS results of the *I*-phase are shown in Table 2.

3.2 Immersion test results

Figure 3 shows the surface morphologies of as-rolled Mg−Zn−Er alloys with corrosion products after immersion in 3.5 wt.% NaCl solution for 3 and 14 d by using SEM, respectively. These Mg−Zn−Er alloys have undergone severe total corrosion damage, and the entire surfaces were covered with insoluble corrosion films. The surfaces of these specimens are covered with thick corrosion products completely, and the products are in morphologies of irregular-type particles (denoted with red circular shape) and needle-like substances (marked with red rectangle shape), as shown in Fig. 3. After immersion for 3 d, it can be found that there are several cavities left on the matrix of Alloy A because of nano-scale *W*-phase (as shown in Fig. 2(a)) which acts as cathode with respect to the anodic action of matrix, where the localized corrosion is activated. There are irregular-type particles and needle-like crystalline compounds on the surface, as shown in Fig. 3(a). Alloy B undergoes higher dissolution than Alloy A, forming several slightly bigger cavities on the surface, and more corrosion products precipitate on the surface, as shown in Fig. 3(c). As the content of Zn further increases, besides the formation of more coarse corrosion products and cavities, lots of white particles precipitate on the surface of Alloys C and D, respectively, as shown in Figs. 3(e) and (g). The presence of coarse second phases (e.g. broken eutectics of *W*-phase or *I*-phase) accelerated the corrosion rate [28]. The as-rolled Mg−*x*Zn−0.5Er alloys show network-like tiny cracks evenly distributed on the surface of these alloys, and the size of cracks increases as the addition of Zn increases. The formation of tiny cracks is due to dehydration of surface after picking out from the immersion solution [29].

Also, the immersion time influences the morphologies of products. Most parts of corrosion products are aggregated into irregular-type (most of them are in spherical-type and blocky-type morphologies, marked by red circular shape) morphologies in Mg−*x*Zn−0.5Er alloys after immersion for 14 d, as shown in Figs. 3(b, d, f, h). The accumulated corrosion products generally cover the matrix, protecting the matrix from further corrosion in some extent [30]. The corrosion products are not dense, and therefore the corrosion reaction is not inhibited effectively under the attack of electrons [3]. A layer of corrosion products is accumulated on the original corrosion products of needle-like crystalline, leading to a wide formation of porous structures in Alloys B, C and D. The cavities and network-like cracks evenly distributed on the whole surface of these alloys get more and larger compared with these in samples after immersion for 3 d (as shown in Figs. 3(a, c, e, g).

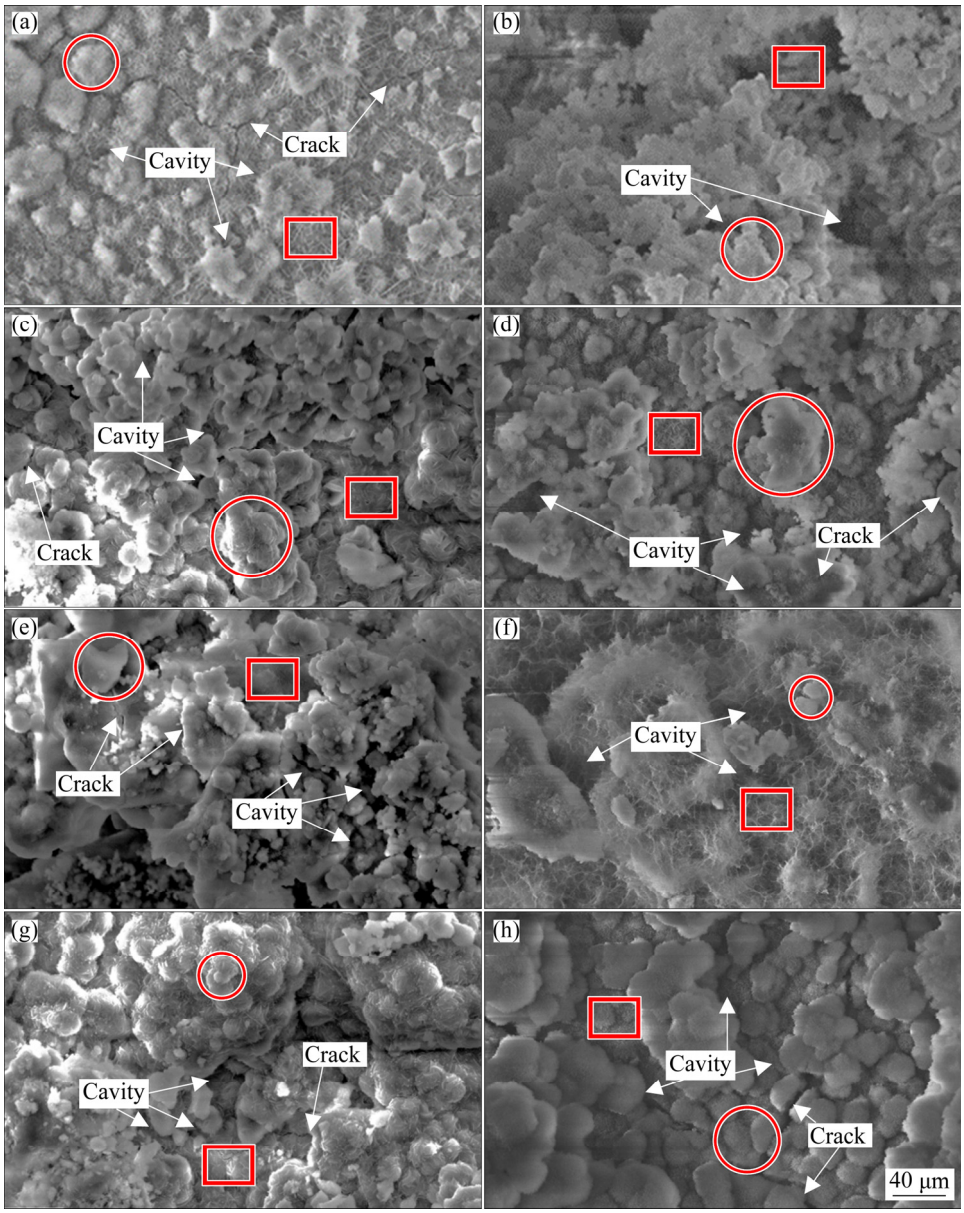

Fig. 3 SEM morphologies of surfaces of Mg−Zn−Er alloys with corrosion products immersed in 3.5 wt.% NaCl solution for 3 d (a, c, e, g) and 14 d (b, d, f, h), respectively: (a, b) Alloy A; (c, d) Alloy B; (e, f) Alloy C; (g, h) Alloy D

The EDS results shown in Figs. 4(b, d, f, h) suggest that the products with needle-like morphology are composed of Mg and O companied with a trace amount of Zn. The molar ratio of O to Mg is close to 2:1, which indicates that the composition of the products is main $Mg(OH)_2$ (The XRD results also confirmed the products of $Mg(OH)_2$, which are not shown in this work).

Figure 5 shows the surface features of these Mg−Zn−Er alloys without corrosion products. Alloy A displays some deep corrosion pits (denoted by white arrows) with a small diameter of 5−10 μm after immersion for 3 d, as shown in Fig. 5(a). The surface feature of Alloy B exhibits larger areas of corrosion attack and corrosion pits. Two kinds of corrosion pits are found on the surface, i.e. deep corrosion pits with a diameter of 5−48 μm and shallow corrosion pits (denoted by white double arrows) with a diameter of 473 μm, as shown in Fig. 5(c), which indicates that Alloy B is suffered from severer corrosion attack than Alloy A. When the contents of Zn are respectively 3 wt.% and 4 wt.%, in the point view of surface, Alloys C and Alloy D are suffered from severer corrosion attack, in which the corrosion reaction occurs on the entire surface, as shown in Figs. 5(e) and (g). We can find lots of shallow corrosion pits (denoted by white double arrows) on the surface, and the sizes of pits

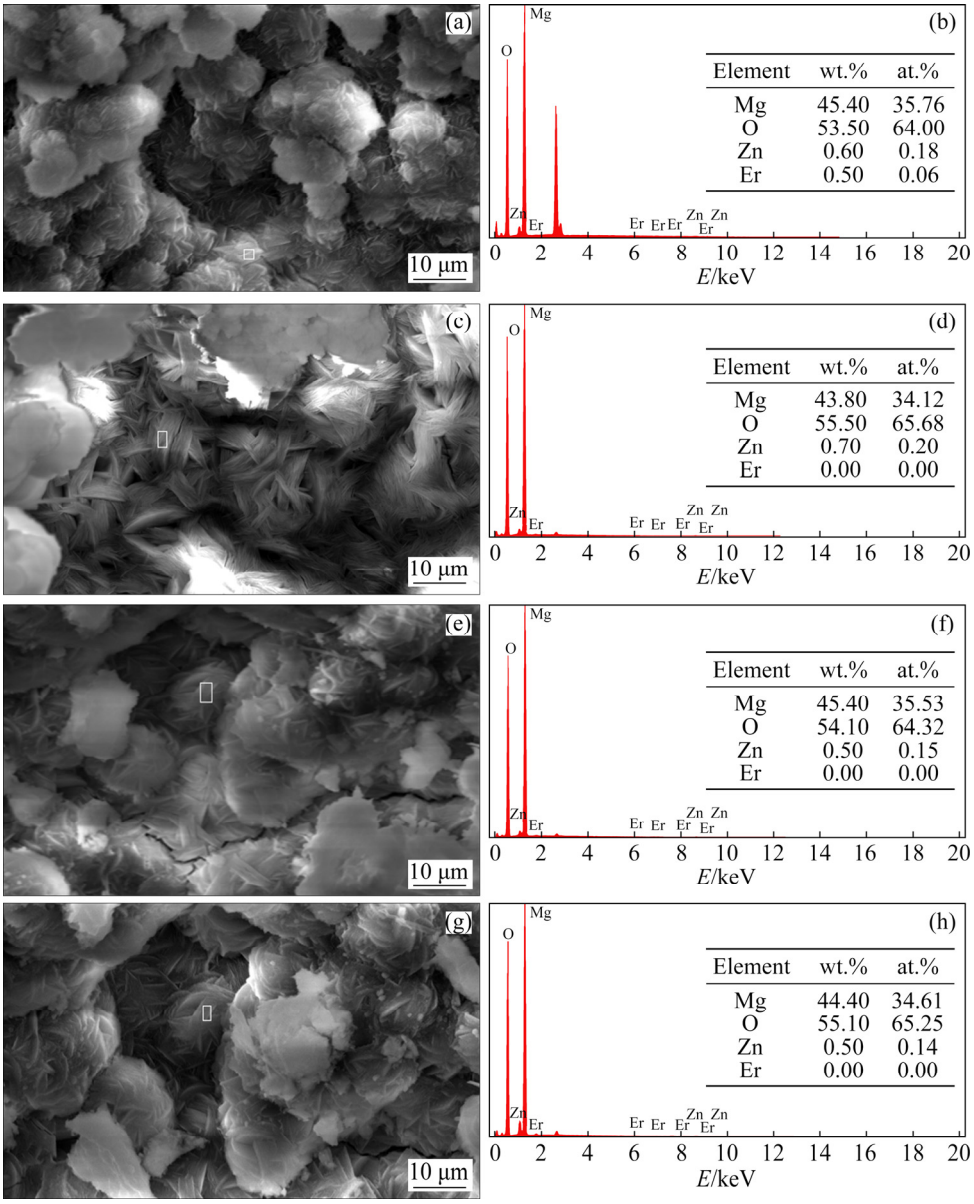

Fig. 4 Surface morphologies of Mg−Zn−Er alloys with corrosion products immersed in 3.5 wt.% NaCl solution for 3 d (a, c, e, g) and corrosponding EDS spectra (b, d, f, h) of white square areas: (a, b) Alloy A; (c, d) Alloy B; (e, f) Alloy C; (g, h) Alloy D

are 109−200 μm in Alloy C and 100−475 μm in Alloy D.

After immersion for 14 d, the surface morphologies of samples without corrosion products are significantly different from these immersed for 3 d, as shown in Figs. 5(b, d, f, h). The corrosion pits get deeper with a larger diameter, compared with those of samples immersed for 3 d. We can find some very deep corrosion pits on the surface of Alloy A, and the diameters of the pits are changed from 109 to 272 μm. This suggests that the corrosion mode is a serious local pitting corrosion due to the content of nano-scale *W*-phase, which is different from the corrosion mode of other Mg−Zn−Er alloys in this work. Other Mg−Zn−Er alloys containing higher levels of Zn show lots of shallow corrosion pits on surface, as shown in Figs. 5(d, f, h). The large shallow corrosion pits are observed on surfaces of Alloy B (diameters of pits: 354−364 μm) and Alloy C (diameters of pits: 300−336 μm), and we can find an obviously uniform corrosion on the entire surface. The homogenous distribution (as shown in Fig. 1 and Fig. 2) of broken *W*-phase and *I*-phase with a relative coarse size is responsible for this corrosion behavior. As the content of Zn increases to 4 wt.%,

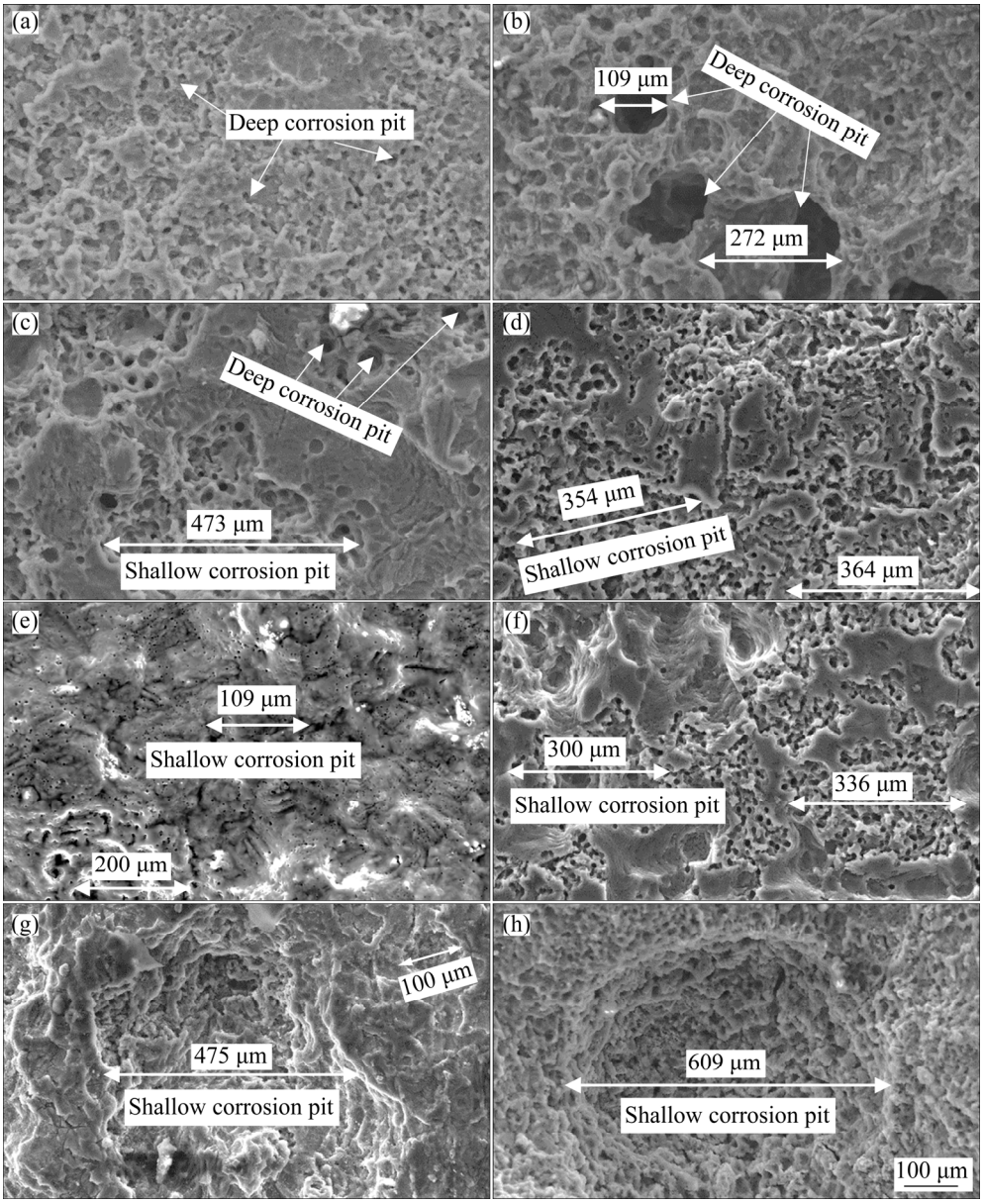

Fig. 5 SEM morphologies of Mg−Zn−Er alloys without corrosion products immersed in 3.5 wt.% NaCl solution for 3 d (a, c, e, g) and 14 d (b, d, f, h): (a, b) Alloy A; (c, d) Alloy B; (e, f) Alloy C; (g, h) Alloy D

the main second phase in Alloy D is coarse broken *I*-phase which is generally distributed at grain boundaries with sizes of 4−20 μm in length and 1.5−8.0 μm in width (as shown in Fig. 1(d)), resulting in formation of larger shallow corrosion pit with a size of ~609 μm. We can conclude from immersion surface morphologies that the corrosion mode transforms from a serious local pitting corrosion to a uniform corrosion because of the variation in kinds of second phases, i.e. *W*-phase, *W*-phase + *I*-phase and *I*-phase.

Figure 6 shows the average corrosion rates of as-rolled Mg−Zn−Er alloys calculated from the mass loss test immersed for 1, 3, 7 and 14 d at room

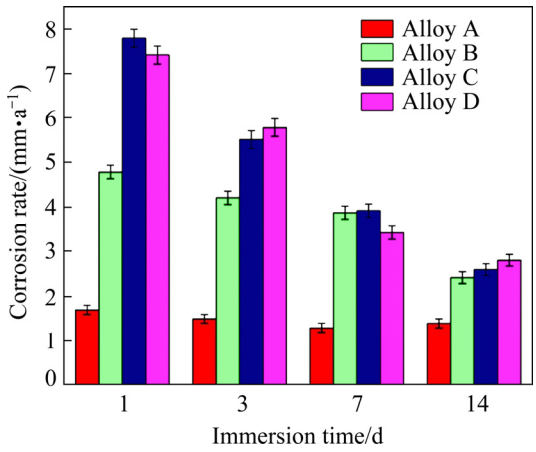

Fig. 6 Corrosion rates obtained by mass loss of Mg−*x*Zn−0.5Er alloys

temperature. The corrosion rate of Mg−Zn−Er alloys has a common feature that the corrosion rate decreases gradually with a prolongation of the immersion time. The corrosion rates of the specimens immersed for 1 d are higher than those immersed for 3, 7 and 14 d, respectively. After immersion for 1 d, the corrosion rates obtained from Alloys A, B, C and D are (1.7±0.10), (4.8±0.15), (7.8±0.21) and (7.4±0.20) mm/a, respectively. Meanwhile, with the expansion of the corrosion damage, the corrosion products gradually increase and gather together to cover the surface of matrix, which further limit corrosion attack, and then the corrosion rate is reduced. The results suggest that the values of the corrosion rate decrease evidently with the prolongation of the immersed time. It is found that the values of the corrosion rate of Alloys A, B, C and D are (1.4±0.10), (2.4±0.13), (2.6±0.14), (2.8±0.13) mm/a after immersion for 14 d, respectively. In addition, the mass loss test results show that Alloy A has a better corrosion resistance than other rest Mg−Zn−Er alloys. It can be inferred that the corrosion behavior is affected by many various factors, especially for the second phase transformation in Mg−Zn−Er alloys.

3.3 Electrochemical test results

Figure 7 shows the polarization curves of Mg−Zn−Er alloys. During the electrochemical reaction, the hydrogen evolution occurs on the cathode of Mg−Zn−Er alloys. The shape of polarization curves of Mg−Zn−Er alloys is relatively symmetrical, and we can find that the increase rate of current density in anodic braches is faster than that of the cathodic branches [31]. The slope of the anodic branches is higher than that of the cathodic branches, which indicates that the cathode process plays a more dominant role in electrochemical corrosion reaction [32]. The curve of Alloy A is at the bottom compared with those of other Mg−Zn−Er alloys, which indicates that the corrosion potential value of Alloy A without voltage loading is the lowest. The corrosion potential values of Alloys B, C and D are similar, and the corrosion potential values increase gradually as the addition of Zn increases. The corrosion potential value of Alloy A is the most negative, which stands for the most positive corrosion tendency, indicating that the addition of Zn makes the potential change positively. The corrosion current density (J_{corr}), corrosion potential (φ_{corr}), anodic Tafel slope (β_a), and cathodic Tafel slope (β_c) were extracted from the polarization curves in Fig. 8. Based on electrochemical parameters (J_{corr}, β_a and β_c), the value of polarization resistance (R_p) was calculated according to the following relationship [33−35]:

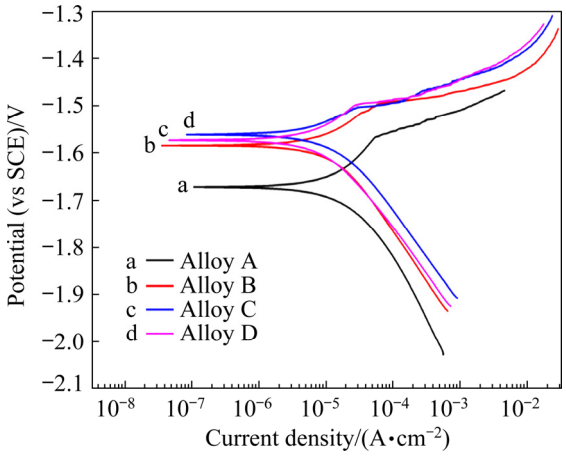

Fig. 7 Potential dynamic polarization curves of Mg−*x*Zn−Er alloys

$$R_p = \frac{\beta_a \beta_c}{2.3(\beta_a + \beta_c) J_{corr}} \quad (2)$$

The relationship between corrosion rate (P_J, mm/a) and current density (J_{corr}, mA/cm^2) is as follows:

$$P_J = 22.85 J_{corr} \quad (3)$$

The electrochemical parameters including J_{corr}, β_a, β_c, P_J and R_p are shown in Table 3. The φ_{corr} is related to the corrosion tendency, and it is not a determinant factor compared with the corrosion current density. The φ_{corr} values observed from Alloys A, B, C and D are (−1.671±0.021), (−1.598±0.018), (−1.610±0.017) and (−1.601±0.015) V, respectively, which indicates that the corrosion resistance has a great relationship with J_{corr} and R_p. The values of R_p decrease and P_J increase as Zn content increases. The values of J_{corr} represent the corrosion resistance of Mg−Zn−Er alloys directly, and the increasing content of Zn leads to a trend of gradual decrease in corrosion resistance of Mg−Zn−Er alloys, which directly stands for the corrosion resistance of these alloys. The results suggest that the corrosion resistance of these alloys is related to the amount of Zn element closely. Also, it is suggested that Alloy A has the best corrosion resistance while Alloy D has the worst corrosion resistance.

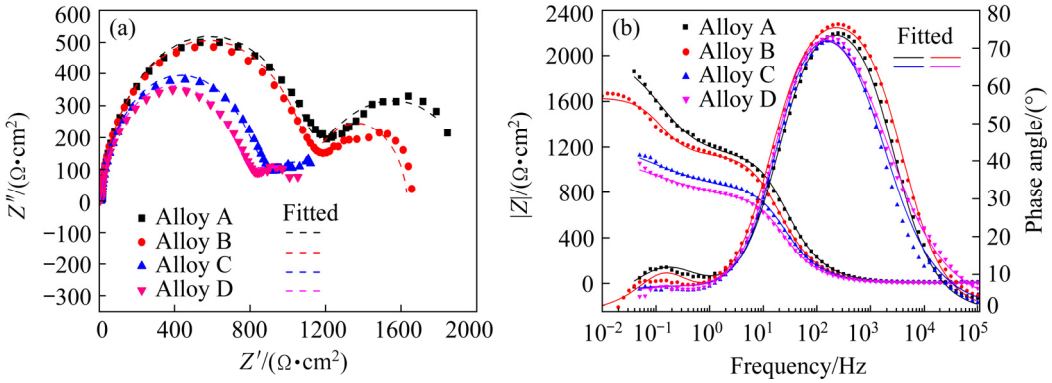

Fig. 8 Electrochemical impedance spectra of Mg−Zn−Er alloys: (a) Nyquist plots; (b) Bode plots

Table 3 Fitting results of polarization curves of Mg−Zn−Er alloys

Alloy	β_a/(mV·dec^{-1})	β_c/(mV·dec^{-1})	φ_{corr}/V	J_{corr}/(μA·cm^{-2})	P_i/(mm·a^{-1})	R_p/kΩ
A	49±5.3	49±3.2	−1.671±0.021	3.76±0.15	0.8592±0.034	2.84±0.11
B	63±9.1	56±5.5	−1.598±0.018	5.55±0.17	1.2682±0.039	2.31±0.20
C	56±8.6	57±4.8	−1.610±0.017	7.73±0.13	1.7663±0.030	1.58±0.16
D	48±6.7	49±5.4	−1.601±0.015	11.41±0.15	2.6187±0.023	0.92±0.10

The electrochemical impedance spectroscopy (EIS) measurement of Mg−Zn−Er alloys was carried out in 3.5 wt.% NaCl solution at an open-circuit potential, and the results are shown in Fig. 8. It is found that Alloys A, B, C, and D contain a capacitance loop in the high frequency range and a capacitance loop in the intermediate frequency range. Also, shapes of impedance spectra are almost similar, which suggest that corrosion mechanisms of Mg−Zn−Er alloys may be the same. Meanwhile, the corrosion rates are different because of the diverse radii of high-frequency capacitive arc resistance. The radii of high-frequency capacitive arc resistance are reduced obviously as Zn content increases from 0.5 wt.% to 4 wt.%. Alloy A has the maximum radius of high-frequency capacitive arc resistance. The diameters of capacitance loops can accurately reflect the charge transfer resistance and corrosion rate of the active corrosion electrode. The larger capacitive resistance diameter indicates that the charge transfer resistance of the active corrosion electrode is larger while the corresponding corrosion rate is smaller [36]. Generally, the high frequency capacitive loop is related to the charge transfer reaction, and the dimension of the capacitive loop determines the charge transfer resistance. The capacitive loop at the middle frequency is attributed to the process of mass transport on surface of the alloy [37,38].

The equivalent circuit shown in Fig. 9 was used for analyzing the EIS spectra of as-rolled Mg−Zn−Er alloys, where R_s is the solution resistance; R_{ct} stands for the charge transfer resistance; CPE_1 represents a constant phase element related to the double-layer capacity. The other constant phase element (CPE_2) and resistance (R_f) are selected to represent the capacitance and resistance of corrosion product film. The fitting results are shown in Table 4. It is found that the R_{ct} value of Alloy A is the highest among these alloys, which suggests that the corrosion rate of this alloy is the lowest. As suggested by the largest value of R_f, the corrosion product film of Alloy A formed during EIS test is more compact compared with that of the rest alloys. In other words, the film has better ability to protect this alloy from corrosion while others have lower ability to escape from corrosion, the results of which are in accordance with immersion and polarization results.

Figure 10 shows the surface morphologies and potentials of Alloy B containing *W*-phase and Alloy *D* containing *I*-phase, respectively. For Alloy B, the

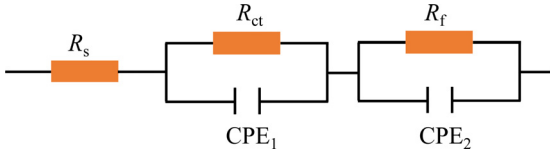

Fig. 9 Equivalent circuit for Alloys A, B, C and D

Table 4 Fitting results of EIS spectra of Mg−Zn−Er alloys

Alloy	R_s/(Ω·cm^2)	R_{ct}/(Ω·cm^2)	CPE$_1$/(10^{-6} F·cm^{-2})	n_1	CPE$_2$/(10^{-6} F·cm^{-2})	n_2	R_f/(Ω·cm^2)	x^2
A	10.6±1.1	1123.3±5.5	10.1±0.4	0.94	15.0±0.5	0.76	911.0±6.6	1.84×10^{-3}
B	5.9±1.4	1107.5±4.1	14.2±0.3	0.93	26.7±0.6	0.94	504.7±4.2	6.27×10^{-3}
C	8.2±1.5	769.7±6.4	13.0±0.3	0.97	26.3±0.6	0.48	602.8±5.3	7.27×10^{-3}
D	5.4±1.2	691.1±5.2	15.1±0.5	0.98	26.9±0.8	0.46	543.4±4.4	1.54×10^{-3}

n_1 and n_2 are dispersion indexes in the range of 0−1. CPE is identical to a pure resistance or a capacitor if n_1 and n_2 are equal to 0 or 1, respectively. x^2 stands for the fitting accuracy, and the smaller the value of x^2 is, the higher the fitting accuracy

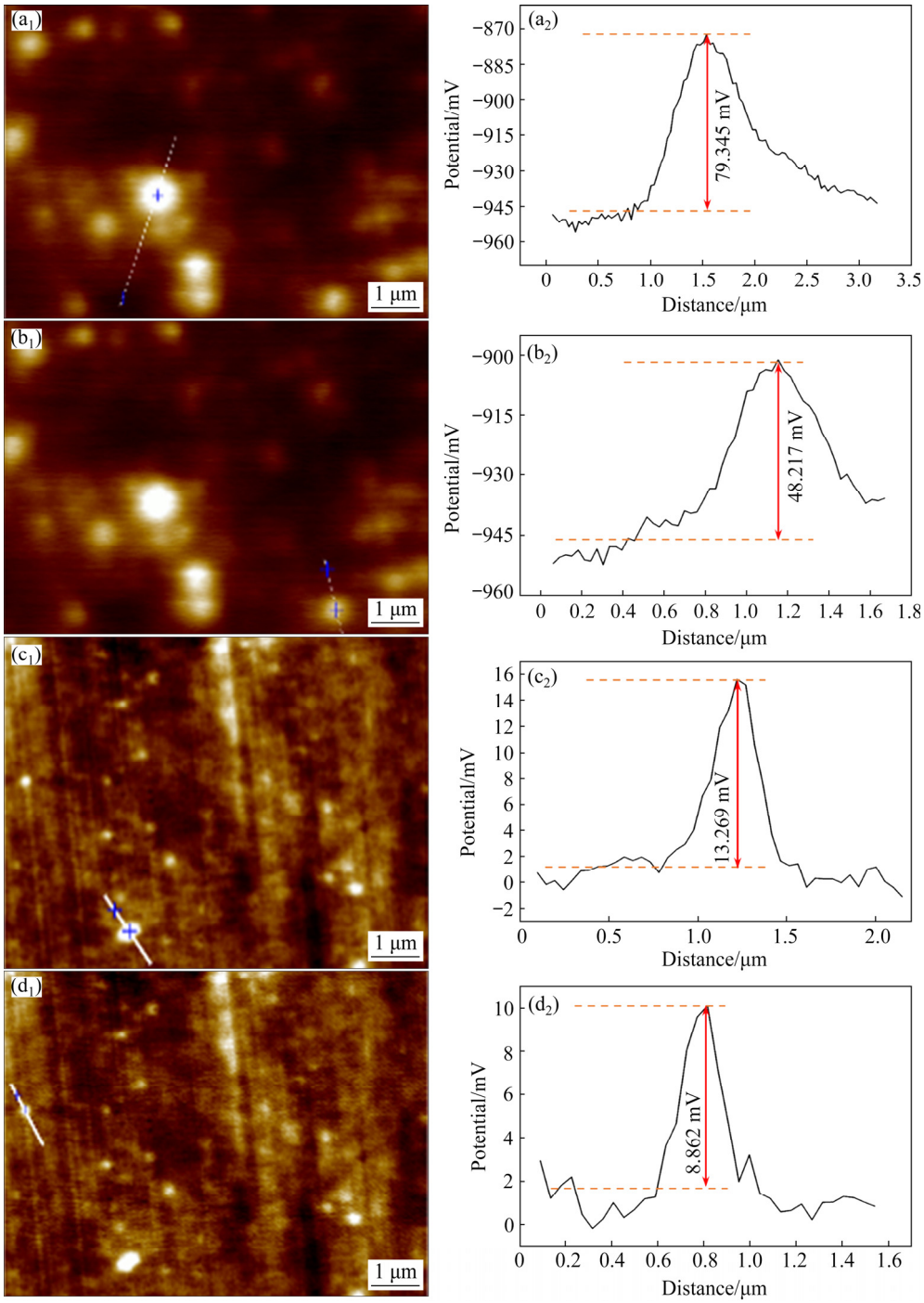

Fig. 10 Surface morphologies (a_1, b_1, c_1, d_1) and potentials (a_2, b_2, c_2, d_2) of Mg−Zn−Er alloys: (a_1, b_1) Two-dimensional morphologies of *W*-phase in Alloy B; (a_2, b_2) Potential curves corresponding to (a_1) and (b_1) in Alloy B, respectively; (c_1, d_1) Two-dimensional morphologies of *I*-phase in Alloy D; (c_2, d_2) Potential curves corresponding to (c_1) and (d_1) in Alloy D, respectively

W-phase marked by short line in Fig. 10(a_1) has a larger size of 717.70 nm, and the local potential difference between *W*-phase and matrix is higher, i.e. 79.345 mV, as shown in Fig. 10(a_2). Meanwhile, the potential value is closely related to the size of the second phase. When the size of the *W*-phase marked by short line in Fig. 10(b_1) decreases to 455.59 nm, the local potential difference between *W*-phase and matrix is about 48.217 mV, as shown in Fig. 10(b_2). In Alloy D, the distribution of *I*-phase is more widespread, and the potential value of *I*-phase is also higher than that of matrix. The local potential difference between *I*-phase (marked by shot line in Fig. 10(c_1) with a size of 412.88 nm) and matrix is about 13.269 mV (Fig. 10(c_2)). The potential value of the *I*-phase with a smaller size of 193.92 nm is about 8.862 mV, as shown in Figs. 10(d_1) and (d_2). Here, we can confirm that the size of the second phase plays an important role in local potential difference between the second phase and matrix as well as its types. The early stage of corrosion observation indicates that severe corrosion will happen firstly around coarse second phases, as shown in Fig. 11, and several deep holes are formed between the second phase and its neighboring matrix after immersion for 30 min,

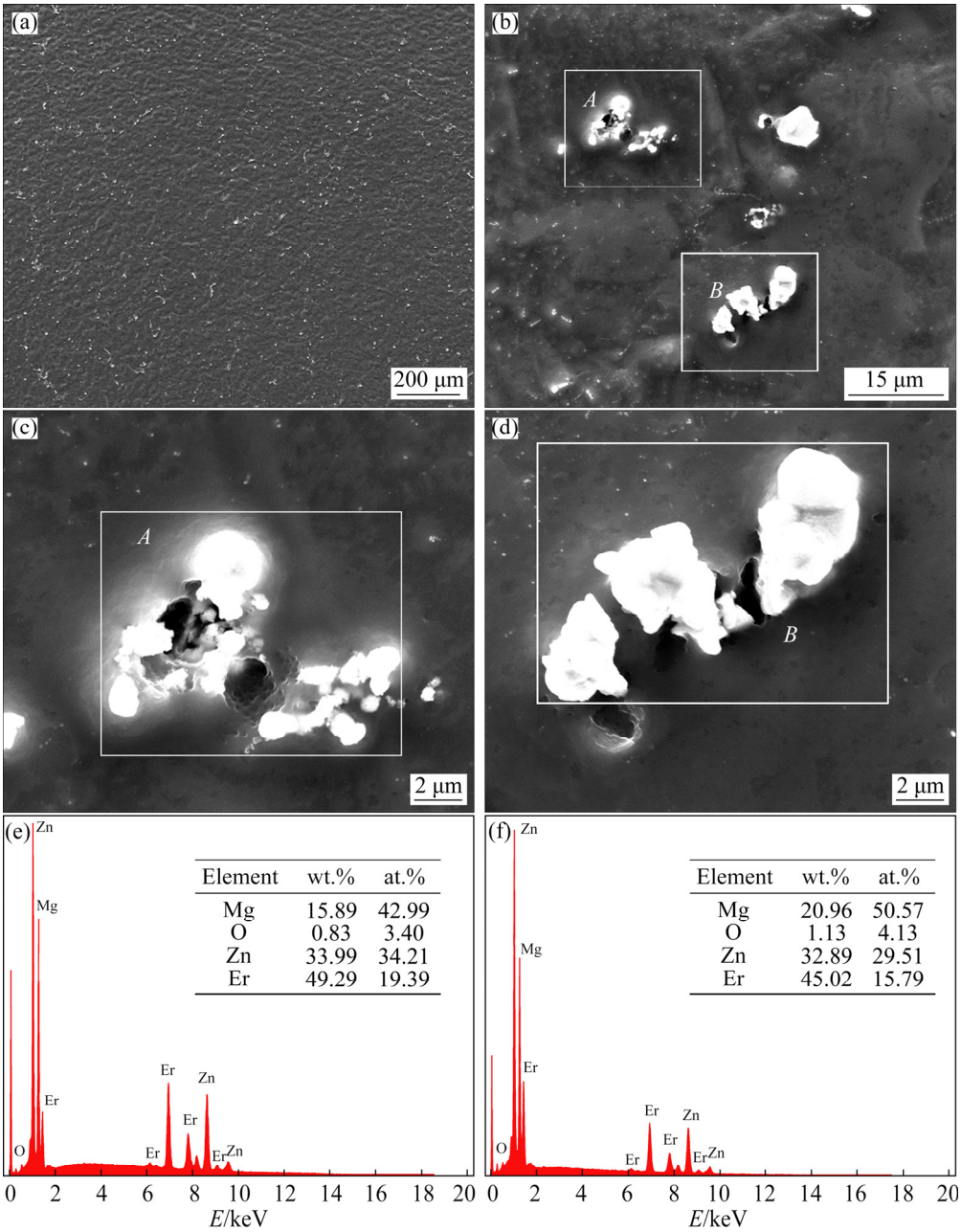

Fig. 11 SEM images of Alloy C immersed for 30 min without corrosion products (a−d) and corresponding EDS analysis results of coarse second phase for Area *A* (e) and Area *B* (f)

whereas no serious corrosion occurs in other regions where some small second phases are located, as shown in Figs. 11(a−d). These coarse second phases are the *W*-phase distributed at grain boundaries (Figs. 11(e) and (f)).

It is considered that the local potential, morphology (size) and distribution of the second phases are the predominant factors affecting the galvanic corrosion of magnesium alloys [39,40]. On the whole, the local potential of the *W*-phase is higher than that of the *I*-phase. The nano-scale *W*-phase usually precipitated at matrix and led to the formation of the deep corrosion pits on the matrix (Fig. 5(b)), standing for an occurrence of the serious local pitting corrosion in Alloy A. However, as the Zn content increased, the coarse *W*-phase or *I*-phase was present, and the broken *W*-phase or *I*-phase was mainly distributed at the grain boundaries, resulting in the formation of the large-size shallow corrosion pits (Fig. 5(h)) because of the preferential corrosion reaction around the coarse second phase (Fig. 11). In order to illustrate the corrosion behavior of these studied alloys, the schematic diagram of the corrosion process is shown in Fig. 12. At the initial stage of corrosion, a kind of $Mg(OH)_2$ film will be formed on the surface of these alloys, playing a significant role in impeding the permeation of corrosion ion and hindering further corrosion process (Figs. 12(a_1) and (b_1)) [41]. But these films are unstable and easy to be destroyed by Cl^- and H_2 as the corrosion continues (Figs. 12(a_2) and (b_2)). The corrosion rate will be accelerated and more products will be formed where most of second phases are located, especially for the coarse second phases in Alloys B, C and D. In addition, the second phase in Alloy A was intragranular *W*-phase with small size, and its local potential value was relatively high, resulting in serious galvanic corrosion, which made the corrosion easier to proceed and led to a deep hole on matrix (Fig. 12(a_3)). In Alloy D, the main second phase was the coarse *I*-phase which was distributed along grain boundaries. The volume fraction of *I*-phase was larger than that of *W*-phase, and the size of *I*-phase in this Alloy D was also larger than that of *W*-phase. As a result, the corrosion pits were more likely to expand during corrosion process in Alloy D (Fig. 12(b_3)).

Obviously, as suggested by the EIS results in Fig. 9, the product films in Alloy A are more protective. It is concluded that the corrosion performance (corrosion rate) of these Mg−*x*Zn−0.5Er alloys is determined by main three factors: volume fraction, morphology (size) and potential difference of the second phases. In addition, the corrosion mode transforms from a serious local pitting corrosion to a uniform corrosion because of such variations in kind and size of the second phases.

4 Conclusions

(1) During the immersion test, the corrosion rates of Mg−*x*Zn−0.5Er alloys were determined by the effects of micro-galvanic corrosion. The types, volume fraction and morphology (size) of the

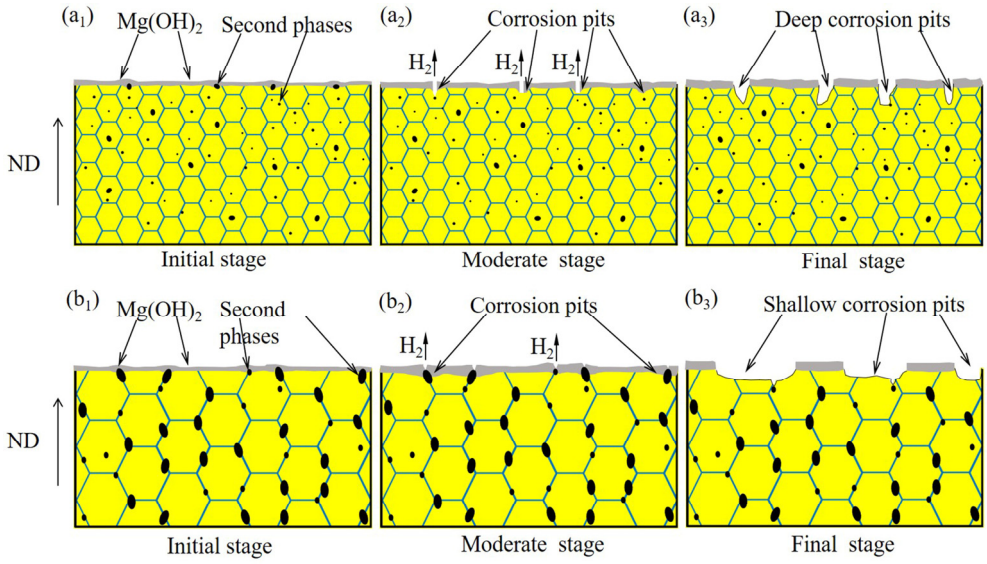

Fig. 12 Schematic diagrams of corrosion process of as-rolled Mg−Zn−Er alloy: (a_1−a_3) Alloy A; (b_1−b_3) Alloy D

second phases played an important role in corrosion performance, and these phases being as cathode to matrix generally accelerated corrosion reaction because of their higher potential than that of matrix. The potential was ascribed to the types and size of the second phases.

(2) The nano-scale *W*-phase (Alloy A) distributed on matrix activated a sharp local pitting corrosion, forming lots of deep corrosion pits. The coarse *W*-phase or *I*-phase mainly located at grain boundaries induced a uniform corrosion, resulting in the formation of shallow corrosion pits. The volume fraction of the coarse second phases in Mg−2.0Zn−0.5Er, Mg−3.0Zn−0.5Er and Mg−4.0Zn−0.5Er alloys, especially in the Mg−4.0Zn−0.5Er alloy, led to a higher corrosion rate.

(3) The long-term immersion (14 d) results indicated that the corrosion resistance decreasing sequence was Mg−0.5Zn−0.5Er (Alloy A) > Mg−2.0Zn−0.5Er (Alloy B) > Mg−3.0Zn−0.5Er (Alloy C) > Mg−4.0Zn−0.5Er alloy (Alloy D).

Acknowledgments

The authors are grateful for the financial supports from Beijing Natural Science Foundation, China (2172013), and the National Key Research and Development Program, China (2016YFB0301101).

References

[1] PAN Hu-cheng, REN Yu-ping, FU He, ZHAO Hong, WANG Li-qing, MENG Xiang-ying, QIN Gao-wu. Recent developments in rare-earth free wrought magnesium alloys having high strength: A review [J]. Journal of Alloys and Compounds, 2016, 663: 321−331.

[2] QIN Gao-wu, REN Yu-ping, HUANG Wei, LI Song, PEI Wen-li. Grain refining mechanism of Al-containing Mg alloys with the addition of Mn−Al alloys [J]. Journal of Alloys and Compounds, 2010, 507(2): 410−413.

[3] SONG Ying-wei, HAN En-hou, DONG Kai-hui, SHAN Da-yong, YIM C D, YOU B S. Study of the corrosion product films formed on the surface of Mg−*x*Zn alloys in NaCl solution [J]. Corrosion Science, 2014, 88: 215−225.

[4] NIINOMI M, NAKAI M. Titanium-based biomaterials for preventing stress shielding between implant devices and bone [J]. International Journal of Biomaterials, 2011, 2011: 836587.

[5] ESMAILY M, SVENSSON J E, FAJARDO S, BIRBILIS N, FRANKEL G S, VIRTANEN S, ARRABAL R, THOMAS S, JOHANSSON L G. Fundamentals and advances in magnesium alloy corrosion [J]. Progress in Materials Science, 2017, 89: 92−193.

[6] JOOST W J, KRAJEWSKI P E. Towards magnesium alloys for high-volume automotive applications [J]. Scripta Materialia, 2017, 128: 107−112.

[7] HU Rong-gang, ZHANG Su, BU Jun-fu, LIN Chang-jian. SONG Guang-ling. Recent progress in corrosion protection of magnesium alloys by organic coatings [J]. Progress in Organic Coatings, 2012, 73(2/3): 129−141.

[8] SONG G, ATRENS A. Understanding magnesium corrosion—A framework for improved alloy performance [J]. Advanced Engineering Materials, 2003, 5: 837−858.

[9] BAHMANI A, ARTHANARI S, SHIN K S. Improvement of corrosion resistance and mechanical properties of a magnesium alloy using screw rolling [J]. Journal of Alloys and Compounds, 2020, 813: 152155.

[10] LAMAKA S V, HÖCHE D, PETRAUSKAS R P, BLAWERT C, ZHELUDKEVICH M L. A new concept for corrosion inhibition of magnesium: Suppression of iron re-deposition [J]. Electrochemistry Communications, 2016, 62: 5−8.

[11] ZHANG S, YUAN G Y, LU C, DING W J. The relationship between $(Mg,Zn)_3RE$ phase and 14H-LPSO phase in Mg−Gd−Y−Zn−Zr alloys solidified at different cooling rates [J]. Journal of Alloys and Compounds, 2011, 509(8): 3515−3521.

[12] THOMAS S, MEDHEKAR N V, FRANKEL G S, BIRBILIS N. Corrosion mechanism and hydrogen evolution on Mg [J]. Current Opinion in Solid State and Materials Science, 2015, 19(2): 85−94.

[13] SAMANIEGO A, GUSIEVA K, LLORENTE I, FELIU S Jr, BIRBILIS N. Exploring the possibility of protective surface oxides upon Mg alloy AZ31 via lutetium additions [J]. Corrosion Science, 2014, 89: 101−110.

[14] GRIMM M, LOHMÜLLER A, SINGER R F, VIRTANEN S. Influence of the microstructure on the corrosion behaviour of cast Mg−Al alloys [J]. Corrosion Science, 2019, 155: 195−208.

[15] ZHU Chen-yang. CHEN Bin. Atomic scale investigation on precipitates and defects of Mg−RE alloys: A review [J]. Advanced Engineering Materials, 2019, 21:1800734.

[16] LU Fu-min, MA Ai-bin, JIANG Jing-hua, GUO Yu, YANG Dong-hui, SONG Dan, CHEN Jian-qing. Significantly improved corrosion resistance of heat-treated Mg−Al−Gd alloy containing profuse needle-like precipitates within grains [J]. Corrosion Science, 2015, 94: 171−178.

[17] LIU Jing, YANG Li-xin, ZHANG Chun-yan, ZHANG Bo, ZHANG Tao, LI Yang, WU Kai-ming. WANG Fu-hui. Significantly improved corrosion resistance of Mg−15Gd−2Zn−0.39Zr alloys: Effect of heat-treatment [J]. Journal of Materials Science & Technology, 2019, 35(8): 1644−1654.

[18] SONG Ying-wei, HAN En-Hou, SHAN Da-yong, YIM Chang-dong YOU Bong-sun. The effect of Zn concentration on the corrosion behavior of Mg−*x*Zn alloys [J]. Corrosion Science, 2012, 65: 322−330.

[19] CAI Shu-hua, LEI Ting, LI Nian-feng, FENG Fang-fang. Effects of Zn on microstructure, mechanical properties and corrosion behavior of Mg−Zn alloys [J]. Materials Science and Engineering C, 2012, 32(8): 2570−2577.

[20] LIU Can-can, ZHENG Hui, GU Xin, JIANG Bai-ling, LIANG Jun. Effect of severe shot peening on corrosion behavior of AZ31 and AZ91 magnesium alloys [J]. Journal of Alloys and Compounds, 2019, 770: 500−506.

[21] YIN Si-qi, DUAN Wen-chao, LIU Wen-hong, WU Liang, YU Jia-min, ZHAO Zi-long, LIU Min, WANG Ping, CUI Jian-zhong, ZHANG Zhi-qiang. Influence of specific second phases on corrosion behaviors of Mg−Zn−Gd−Zr alloys [J]. Corrosion Science, 2020, 166: 108419.

[22] SONG G L, ATRENS A, DARGUSCH M. Influence of microstructure on the corrosion of diecast AZ91D [J].

Corrosion Science, 1998, 41(2): 249−273.
[23] ZHANG Xiao-bo, WANG Qian, CHEN Feng-bin, WU Yu-juan, WANG Zhang-zhong, WANG Qiang. Relation between LPSO structure and biocorrosion behavior of biodegradable GZ51K alloy [J]. Materials Letters, 2015, 138: 212−215.
[24] CHINO Y, HUANG X S, SUZUKI K, SASSA K. MABUCHI M. Influence of Zn concentration on stretch formability at room temperature of Mg−Zn−Ce alloy [J]. Materials Science and Engineering A, 2010, 528(2): 566−572.
[25] BASU I, AL-SAMMAN T. Twin recrystallization mechanisms in magnesium-rare earth alloys [J]. Acta Materialia, 2015, 96: 111−132.
[26] SINGH A, BASHA D A, SOMEKAWA H, TSUCHIYA K. Nucleation of recrystallized magnesium grains over quasicrystalline phase during severe plastic deformation of a Mg−Zn−Y alloy at room temperature [J]. Scripta Materialia, 2017, 134: 80−84.
[27] KWAK T Y, KIM W J, Effect of refinement of grains and icosahedral phase on hot compressive deformation and processing maps of Mg−Zn−Y magnesium alloys with different volume fractions of icosahedral phase [J]. Journal of Materials Science & Technology, 2019, 35(1): 181−191.
[28] FENG Hui, LIU Shu-hong, DU Yong, LEI Ting, ZENG Rong-chang, YUAN Tie-chui. Effect of the second phases on corrosion behavior of the Mg−Al−Zn alloys [J]. Journal of Alloys and Compounds, 2017, 695: 2330−2338.
[29] BAKHSHESHI-RAD H R, ABDUL-KADIR M R, IDRIS M H, FARAHANY S. Relationship between the corrosion behavior and the thermal characteristics and microstructure of Mg−0.5Ca−*x*Zn alloys [J]. Corrosion Science, 2012, 64: 184−197.
[30] SONG Ying-wei, HAN En-hou, DONG Kai-hui, SHAN Da-yong, YIM Chang-Dong, YOU Bong-Sun. Microstructure and protection characteristics of the naturally formed oxide films on Mg−*x*Zn alloys [J]. Corrosion Science, 2013, 72: 133−143.
[31] ZHAO Ming-chun, LIU Ming, SONG Guang-ling, ATRENS A. Influence of pH and chloride ion concentration on the corrosion of Mg alloy ZE41 [J]. Corrosion Science, 2008, 50(11): 3168−3178.
[32] WANG S D, XU D K, CHEN X B, HAN E H, DONG C. Effect of heat treatment on the corrosion resistance and mechanical properties of an as-forged Mg−Zn−Y−Zr alloy [J]. Corrosion Science, 2015, 92: 228−236.
[33] ARGADE G R, KANDASAMY K, PANIGRAHI S K, MISHRA R S. Corrosion behavior of a friction stir processed rare-earth added magnesium alloy [J]. Corrosion Science, 2012, 58: 321−326.
[34] LIU M, SCHMUTZ P, UGGOWITZER P J, SONG G L, ATRENS A. The influence of yttrium (Y) on the corrosion of Mg−Y binary alloys [J]. Corrosion Science, 2010, 52(11): 3687−3701.
[35] ARRABAL R, PARDO A, MERINO M C, MOHEDANO M, CASAJÚS P, PAUCAR K, GARCÉS G. Effect of Nd on the corrosion behaviour of AM50 and AZ91D magnesium alloys in 3.5 wt.% NaCl solution [J]. Corrosion Science, 2012, 55: 301−312.
[36] WU Guo-song, FENG Kai, SHANAGHI A, ZHAO Ying, XU Rui-zhen, YUAN Guang-yin, CHU PAUL K. Effects of surface alloying on electrochemical corrosion behavior of oxygen-plasma-modified biomedical magnesium alloy [J]. Surface and Coatings Technology, 2012, 206(14): 3186−3195.
[37] JAMESH M, KUMAR S, SANKARA NARAYANAN T S N. Corrosion behavior of commercially pure Mg and ZM21 Mg alloy in Ringer's solution—Long term evaluation by EIS [J]. Corrosion Science, 2011, 53(2): 645−654.
[38] ZHANG Yuan, LI Jian-xing, LI Jing-yuan. Effects of microstructure transformation on mechanical properties, corrosion behaviors of Mg−Zn−Mn−Ca alloys in simulated body fluid [J]. J Mech Behav Biomed Mater, 2018, 80: 246−257.
[39] MIAO Hong-wei, HUANG Hua, SHI Yong-juan, ZHANG Hua, PEI Jia, YUAN Guang-yin. Effects of solution treatment before extrusion on the microstructure, mechanical properties and corrosion of Mg−Zn−Gd alloy in vitro [J]. Corrosion Science, 2017, 122: 90−99.
[40] LIU Jing, YANG Li-xin, ZHANG Chun-yan, ZHANG Bo, ZHANG Tao, LI Yang, WU Kai-ming, WANG Fu-hui. Role of the LPSO structure in the improvement of corrosion resistance of Mg−Gd−Zn−Zr alloys [J]. Journal of Alloys and Compounds, 2019, 782: 648−658.
[41] GUO Xing-wu, CHANG Jian-wei, HE Shang-ming, DING Wen-jiang, WANG Xi-shu. Investigation of corrosion behaviors of Mg−6Gd−3Y−0.4Zr alloy in NaCl aqueous solutions [J]. Electrochimica Acta, 2007, 52(7): 2570−2579.

轧制态 Mg−Zn−Er 合金板材的显微组织及腐蚀行为

刘 轲，娄 峰，付军健，于子健，李淑波，王朝辉，杜 宪，杜文博

北京工业大学 材料与制造学部，北京 100124

摘 要：对轧制态 Mg−*x*Zn−0.5Er (*x* = 0.5, 2.0, 3.0, 4.0, 质量分数，%)合金的腐蚀行为和机理进行研究。结果表明，第二相与基体之间的电位差由第二相的种类和尺寸决定。Mg−0.5Zn−0.5Er 合金基体中占主导地位的纳米尺寸 *W* 相引起合金局部尖锐点蚀。但是，随着粗大 *W* 相或 *I* 相体积分数的增加，腐蚀反应优先在粗大 *W* 相或 *I* 相附近发生，腐蚀更加均匀，腐蚀速率加快。长期浸泡(14 d)结果表明，合金耐蚀性由高到低的顺序为 Mg−0.5Zn−0.5Er > Mg−2.0Zn−0.5Er > Mg−3.0Zn−0.5Er > Mg−4.0Zn−0.5Er。

关键词：镁合金；第二相；显微组织；腐蚀行为

(Edited by Wei-ping CHEN)